SANDIA REPORT

SAND2019-0865
Unlimited Release
Printed January 24, 2019

An approach for shear-stress based scour prediction

Ryan G. Coe, Alice G. Gillespie, Chris Chartrand, Mike Morrow, Mike Delos-Reyes, Fabian Wendt, Yi-Hsiang Yu, Tuba Oskan-Haller, Pedro Lomonaco, Jesse Roberts, Sterling Olson, and Craig Jones

Prepared by
Sandia National Laboratories
Albuquerque, New Mexico 87185 and Livermore, California 94550

Sandia National Laboratories is a multimission laboratory managed and operated by National Technology and Engineering Solutions of Sandia, LLC., a wholly owned subsidiary of Honeywell International, Inc., for the U.S. Department of Energy's National Nuclear Security Administration under contract DE-NA0003525.

Sandia National Laboratories

Issued by Sandia National Laboratories, operated for the United States Department of Energy by National Technology and Engineering Solutions of Sandia, LLC.

Available to DOE and DOE contractors from
U.S. Department of Energy
Office of Scientific and Technical Information
P.O. Box 62
Oak Ridge, TN 37831

Telephone: (865) 576-8401
Facsimile: (865) 576-5728
E-Mail: reports@adonis.osti.gov
Online ordering: http://www.osti.gov/bridge

Available to the public from
U.S. Department of Commerce
National Technical Information Service
5285 Port Royal Rd
Springfield, VA 22161

Telephone: (800) 553-6847
Facsimile: (703) 605-6900
E-Mail: orders@ntis.fedworld.gov
Online ordering: http://www.ntis.gov/help/ordermethods.asp?loc=7-4-0#online

SAND2019-0865
Unlimited Release
Printed January 24, 2019

An approach for shear-stress based scour prediction

Abstract

Scour beneath seafloor pipelines, cables, and other offshore infrastructure is a well-known problem. Recent interest in seafloor mounted wave energy converters brings another dynamic element into the traditional seafloor scour problem. In this paper, we consider the M3 Wave APEX device, which utilizes airflow between two flexible chambers to generate electricity from waves. In an initial at-sea deployment of a demonstration/experimental APEX in September 2014 off the coast of Oregon, scour beneath the device was observed. As sediment from the beneath the device was removed by scour, the device's pitch orientation was shifted. This change in pitch orientation caused a degradation in power performance. Characterizing the scour associated with seafloor mounted wave energy conversion devices such as the M3 device is the objective of the present work.

1 Introduction

This report focuses on the investigation of scour beneath the M3 WAVE APEX wave energy converter (WEC). The pressure differential concept for a WEC, as implemented in the M3 design, is based on two flexible air-bags that are connected through a tube [1]. The bags inflate and deflate, depending on the local wave induced forces on the bags. This triggers a flow though the connecting tube. A turbine in the middle of the tube is driven by this airflow and produces electrical power.

In an initial at-sea deployment of a demonstration/experimental APEX in September 2014 off the coast of Oregon, scour beneath the device was observed. As sediment from the beneath the device was removed by scour, the device's pitch orientation was shifted. This change in pitch orientation caused a degradation in power performance.

To assess scour for the APEX device (as well as future similar devices), numerical and experimental efforts were undertaken. First, two different causes of scour for the APEX were considered: wave induced/diffracted flow and radiated flow due to the motion of the APEX device. Next, using the canonical scour system of oscillatory two-dimensional flow over a pipe, a relationship based on local shear stress on the sea bed was developed. Experiments with a series of APEX-like devices were carried out to assess scour. Predictions from this formulation were compared with experimental results show good agreement on local scour depth and overall scour area.

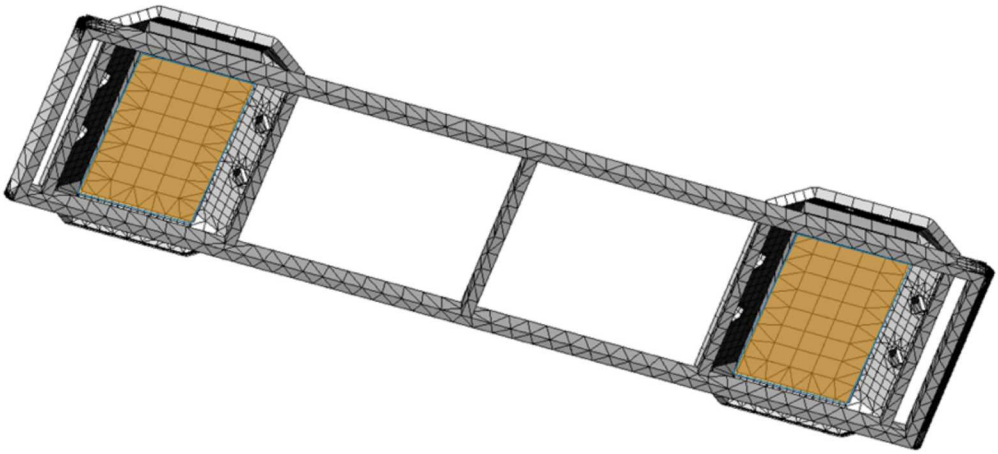

Figure 1: M3 WAVE APEX device geometry used for WAMIT Model.

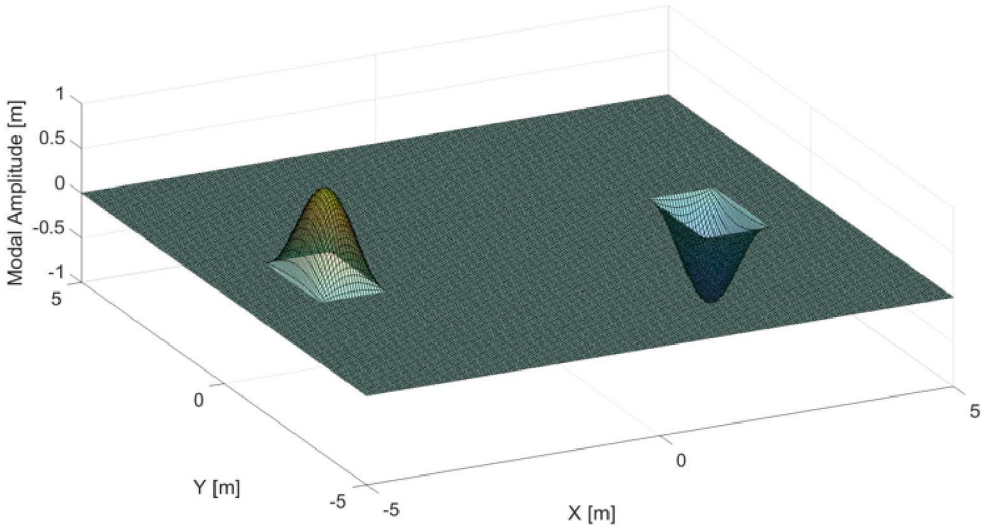

Figure 2: Mode Shape introduced to consider bag motion in WAMIT model.

2 Generalized modes analysis

To assess the importance of radiated versus incident/diffracted flow for scour, the M3 Apex device was modeled within WAMIT [4]. This approach can be used to assess the relative importance of radiated versus incident/diffracted flow, but does not include viscous effects. Thus WAMIT was not used in this study to directly predict scour.

The flexible bag motion of the APEX was considered through the introduction of one additional generalized mode. The utilized surface mesh is shown in Figure 1. The additional mode shape used to represent the bag motion is shown in Figure 2. This mode shape is applied to the bottom surfaces of the flexible bags, highlighted in orange in Figure 1. No additional stiffness/mass/damping were associated with the introduced bag deformation mode.

Table 1: Wave regimes used in WAMIT analyses.

Regime	$T_{p,1}$ [s]	$T_{p,2}$ [s]	$H_{s,1}$ [m]	$H_{s,2}$ [m]
1	16.3	6.92	0.38	0.49
2	8.33	14.44	0.90	0.37
3	11.11	4.47	0.30	0.31
4	13.07	20.00	1.04	0.50

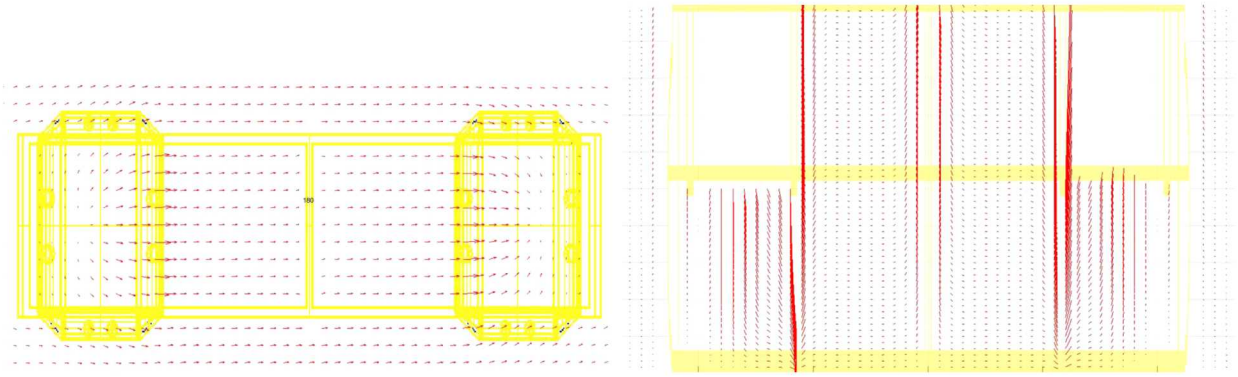

(a) Peak 1 (b) Peak 2

Figure 3: Flow field around APEX device predicted by WAMIT for Regime 3..

Four bimodal wave regimes that occurred during the Apex Oregon deployment were been selected for analysis with WAMIT (Table 1). The APEX device was simulated in WAMIT using these four selected wave regimes. The flow field around the body was requested as output and further analyzed in terms of scouring potential. The resulting flow field around the device is visualized at the seabed level in Figure 3a and at a length-wise cross section along the center in Figure 3b) for Regime 3.

The maximum velocities occur at the gap between seabed and caisson (orange circles in Figure 3). The simulation was repeated with a rigid bag and the flow fields with and without flexible bags were compared (Figure 4). In conclusion, the influence of the bag motion on flow field close to seabed appears to be relatively small and is therefore not considered a driving factor for any potential scouring.

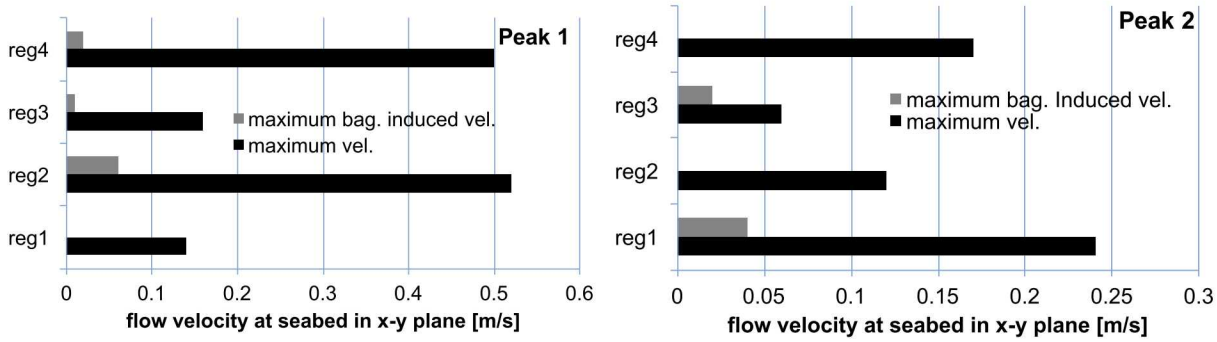

(a) Peak 1

(b) Peak 2

Figure 4: Maximum flow velocities at seabed.

3 Defining an empirical scour trend

A number of studies have used computational fluid dynamics (CFD) to predict scour. Generally, the methods developed use some sort of iterative/coupled approach to allow for scour to develop (see, e.g., [2, 5]. Geometries in the CFD simulations are thus deformed to represent the scour process. This allows the flow field to respond, just as in a real scour process.

In this study, we have purseud a method which might approximate/predict scour with fewer computational resources. For this purpose, we utilized shear stress on the sea floor (e.g., from a CFD simulation) to predict scour underneath an arbitrary geometry, we have examined the flow over a 2-dimensional (2D) pipe. The relationship derived via this canonical case can then be extended to arbitrary geometries. The 2D pipe flow problem is well-studied and empirical data has shown a strong trend [3].

$$\frac{S}{D} = 0.1\sqrt{KC} \tag{1}$$

The Kluegan-Carpenter number, KC, is given by

$$KC = \frac{UT}{D}. \tag{2}$$

Similarly to the trend given by (1), the scour width for 2D pipe flow follows. [1]

$$\frac{W}{D} = 0.35KC^{0.65} \tag{3}$$

Knowing that scour is highly dependent on KC, it is desirable to define an empirical trend that will allow local scour to be predicted by some function of KC. We thus define local Kluegan-Carpenter number as

$$KC(x,y) = \frac{T}{D}\left(\frac{\tau(x,y) - \tau_\infty}{\rho U_m}\right). \tag{4}$$

Here, T is the wave period. The parameter D is some representative dimension of the body of interest. The local shear stress is given by $\tau(x,y)$ and τ_∞ is the far field shear stress. The water density is given by ρ and the far field flow velocity is U_m.

In addition to KC, scour in waves is known to be influenced by turbulence levels. By monitoring the turbulence level just above the floor, we can write

[1] In the development of this work, a set of simulations were conducted to investigate 2D pipe scour. A summary of these results is presented in Appendix A.

$$D_{TKE}(x,y) = \frac{D\sqrt{f_{\text{cal}} TKE(x,y)}}{U_m}. \tag{5}$$

Here, $TKE(x,y)$ is the turbulent kinetic energy level averaged over one period taken at 1 cm above the floor. The tuning parameter f_{cal} will be defined momentarily.

Using (4) and (5), the local scour can be predicted by

$$S(x,y) = D_{TKE}(x,y)\sqrt{KC(x,y)} - S_\infty, \tag{6}$$

where S_∞ is the far field scour. The tuning parameter f_{cal} in (5) can be set based on the known solution for 2D pipe flow.

$$f_{\text{cal}}(H_s, T_p) = \text{argmin}\left(\left|\max(S(x,y)) - S_{\text{pipe}}\right|\right) \tag{7}$$

Here, S_{pipe} is the scour depth prediction from (1).

Table 2: Wave conditions for comparison between CFD scour prediction and experimental data.

Wave ID	Height, H [m]	Period, T [s]	Wave length, λ [m]
1	0.30	3.6	15.9
2	0.30	5.8	28.2
3	0.60	3.6	15.9
4	0.60	5.8	28.2

4 Results

A series of experiments were run in the Oregon State University (OSU) Large Wave Flume using scale models of APEX and sand. The flume is 104 m long and 3.7 m wide. For these tests, a water depth of 2.7 m was used. Waves in the flume are produced by a piston-type wave maker. Table 2 list the wave conditions considered here.

For each wave, sonar was used to measure the local scour before and after running waves. The difference between the measurements was taken to find the scour created during the experiment. The resulting surfaces are shown in Figure 5. CFD simulations were run to correspond with each wave.

To provide a comparison between the experimental and CFD-based scour results, a longitudinal transect was taken down the center of the APEX device. Thus, the local scour ($S(x, y = 0)$) can be plotted from both the experiment and CFD prediction. The resulting comparison is shown for each wave from Table 2 in Figure 6.

Overall, the comparisons shown in Figure 6 display good agreement between the CFD scour prediction and the experimental results. The predictions in Wave 1 and Wave 2 are best. Here, the local scour depth prediction matches the experiment quite well. The prediction perform worse in Waves 3 and 4, which have double the amplitude of Waves 1 and 2. However, even when the CFD scour prediction is poor (in Waves 3 and 4), while the local scour depth may not be well-predicted, the extents of the scour tend to match fairly well.

One factor that may have affected the results is the presence of some non-zero initial scour. In the case of Wave 4 the initial scour was quite large, which may have compromised the experiment. Also, the device may not always have been located exactly the same in the experimental and numerical tests.

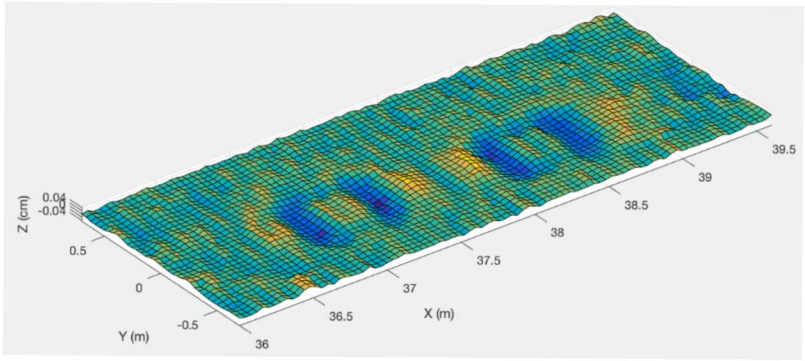

(a) Wave 1

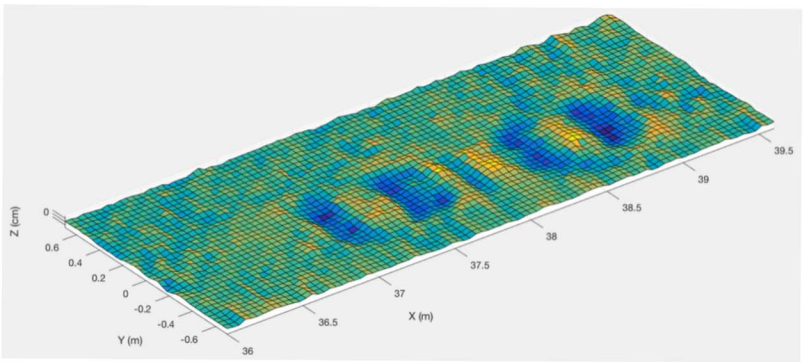

(b) Wave 2

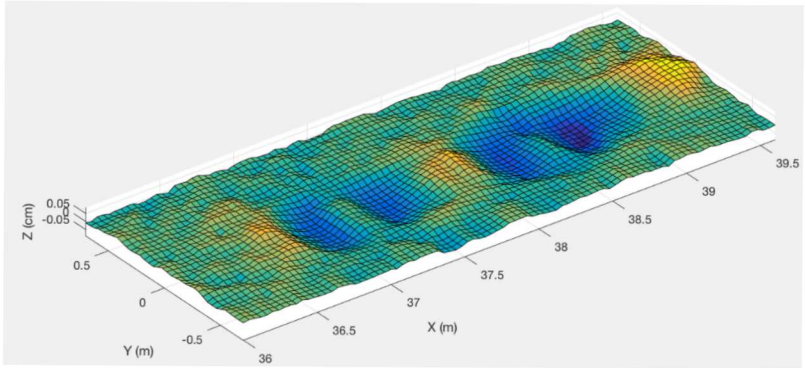

(c) Wave 3

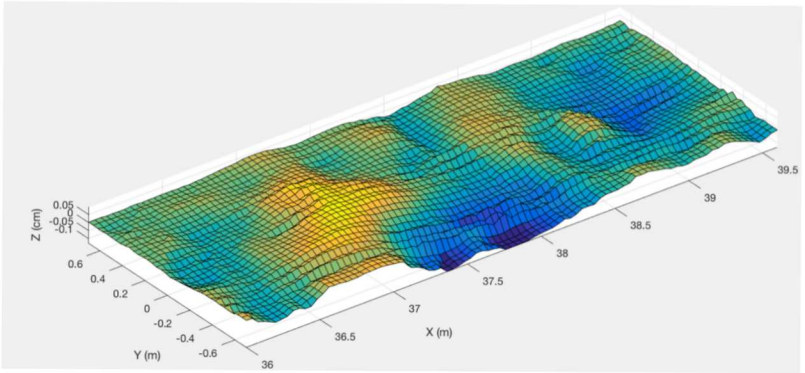

(d) Wave 4

Figure 5: Experimental measured scour for APEX device.

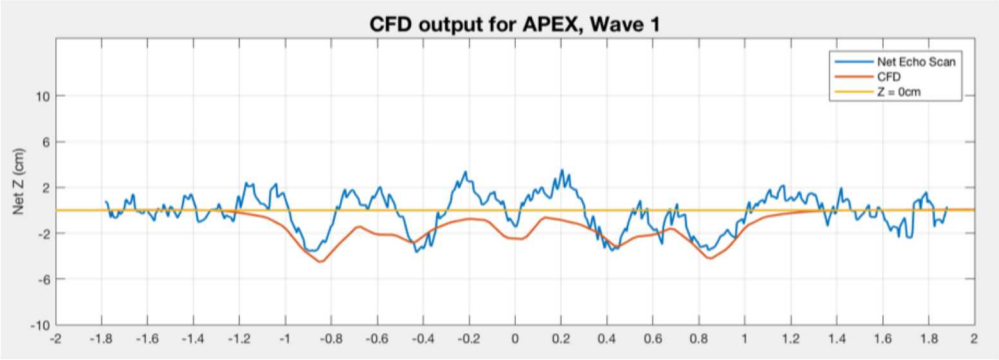

(a) Wave 1

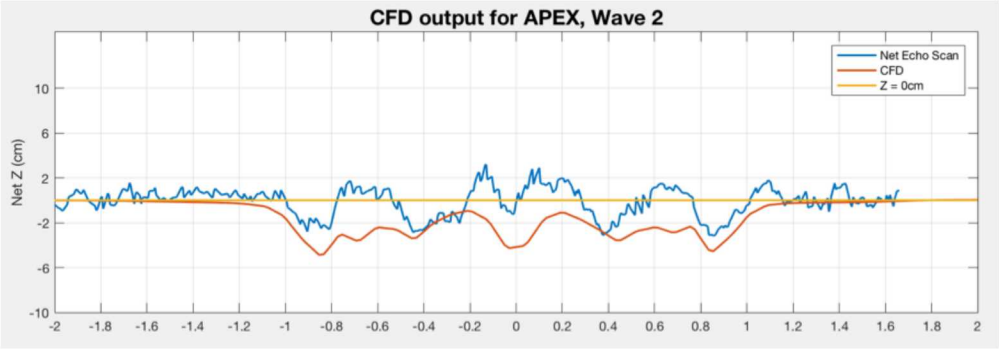

(b) Wave 2

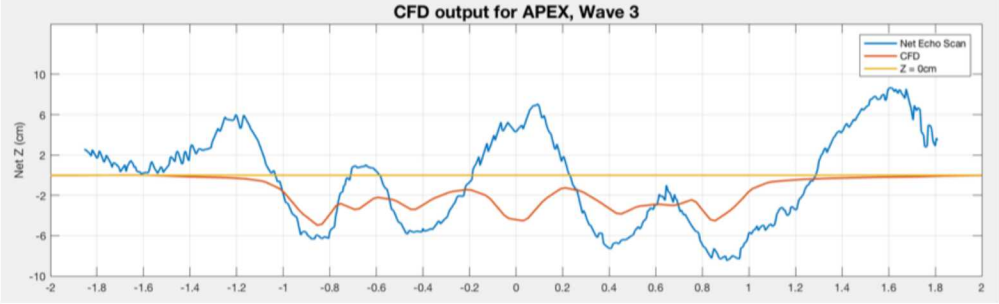

(c) Wave 3

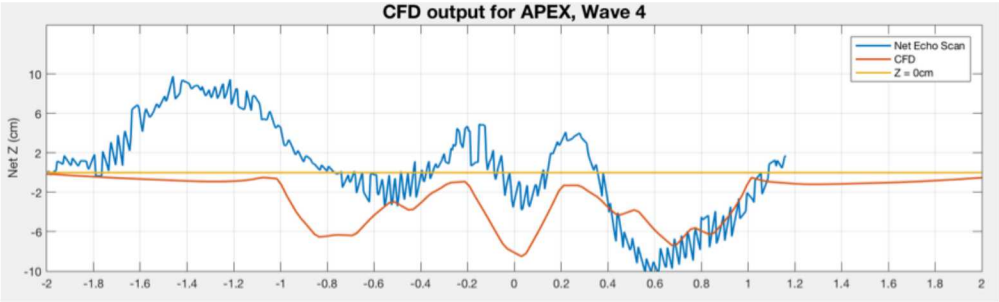

(d) Wave 4

Figure 6: Comparison of scour from experiment and CFD prediction using (6) for APEX device. Plot of longitudinal transect of scour depth.

5 Conclusion

A model for scour depth as a function of periodic flow parameters has been developed by relating the shear stress results of CFD simulations to an empirical relationship derived from experiments. A strong trend was established for a canonical system with a large amount of experimental data available. This formulation was then expanded to incorporate local turbulence levels, which are a known driver of scour.

The resulting model was compared with experiments conducted with sand in a wave flume. A comparison with experimental data showed good results. In some cases, the local scour depth is well-predicted. On other cases, where local scour depth is not well-predicted, the extents of the scour area around the device predicted by the CFD simulation match fairly well with the experimental results.

Based on this initial analysis, the method developed in this study represents a feasible engineering method for predicting scour beneath an arbitrary body in waves. Note that scour is fundamentally nonlinear process: the flow field redistributes sediment, which in turn changes the flow field. Thus the method considered in this study, which does not allow for deformation of the floor, is a linear approximation of this phenomenon. Future work should look at a wider range of wave conditions and consider a variety of devices/bodies.

References

[1] Aurélien Babarit, Fabian Wendt, Y-H Yu, and Jochem Weber. Investigation on the energy absorption performance of a fixed-bottom pressure-differential wave energy converter. *Applied Ocean Research*, 65:90–101, 2017.

[2] Nils RB Olsen and Morten C Melaaen. Three-dimensional calculation of scour around cylinders. *Journal of Hydraulic Engineering*, 119(9):1048–1054, 1993.

[3] B Mutlu Sumer and Jørgen Fredsøe. *The mechanics of scour in the marine environment*. World Scientific, Singapore, 2002.

[4] WAMIT. *WAMIT User Manual*. Chestnut Hill, MA, 7 edition, 2012.

[5] Wen Xiong, CS Cai, Bo Kong, and Xuan Kong. Cfd simulations and analyses for bridge-scour development using a dynamic-mesh updating technique. *Journal of Computing in Civil Engineering*, 30(1):04014121, 2014.

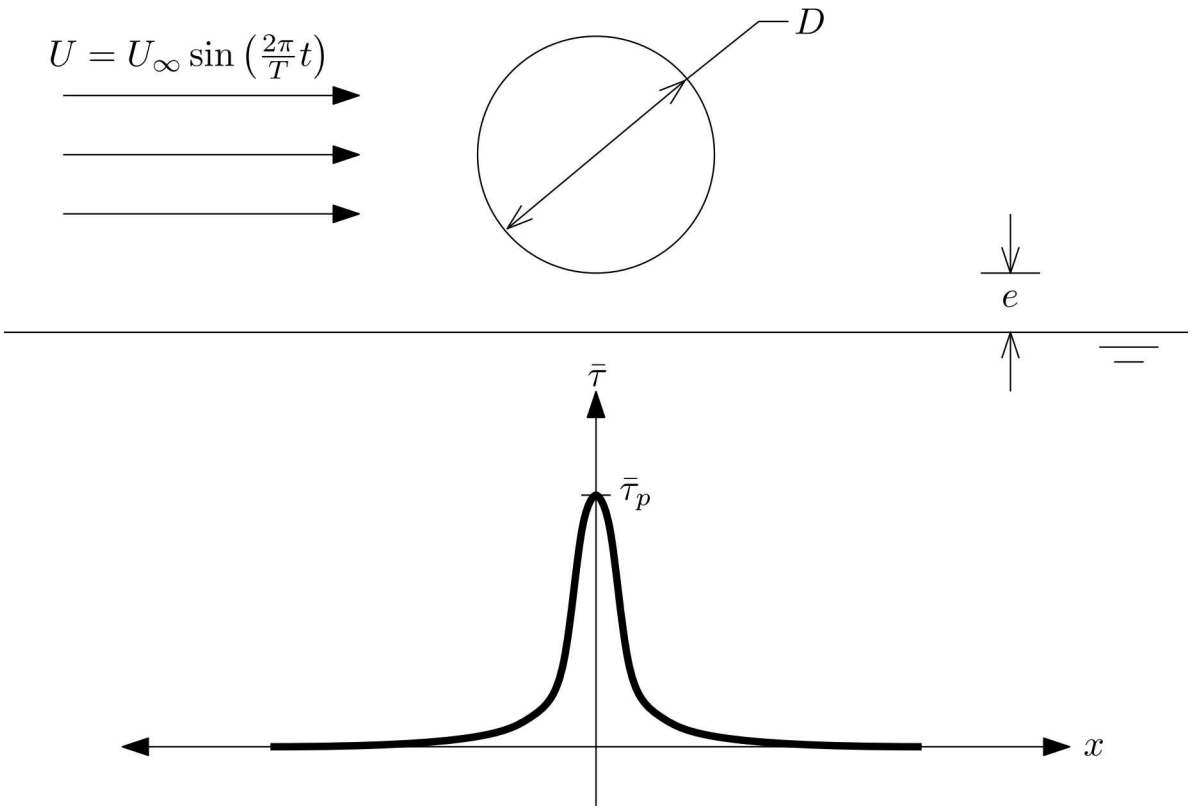

Figure A.1: Diagram of 2D flow over pipe simulation with shear stress map.

A Investigating 2D pipe scour

CFD simulations were conducted in OpenFOAM using the configuration depicted in Figure A.1 for a variety of *KC* numbers. The unsteady RANS simulations were run with using the `pimpleFoam` solver with an adjustable timestep that enforced the condition $CFL < 0.25$ throughout the entire domain. The computational grid was generated in Pointwise with a wall spacing set to $\Delta x_{wall} = 0.005D$, expanding out to a far field discretization of $\Delta x_{far} \approx D$. Illustrations of the grid used for one of the $D = 2$ simulations are shown in Figures A.2 and A.3. Example results from a simulation are shown in Figure A.4.

Here, oscillating flow, with a velocity of $U = U_\infty \sin\left(\frac{2\pi}{T}t\right)$, is simulated over a cylinder with diameter D. As some 2D pipe scour (that which is due to jetting beneath the pipe) is initiated by a pressure differential, not shear stress, the simulation is configured with a cylinder offset from the sea floor by some small distance e, which varied between $0.025D$ and $0.2D$ in these simulations. The simulation configuration depicted in Figure A.1 was evaluated by finding the period-averaged shear stress, $\bar{\tau}$, along the stream-wise dimension, x (see lower half of Figure A.1). From the averaged shear stress, the peak value of the distribution, $\bar{\tau}_p$, is extracted.

A series of simulations were run with varying values of *KC*. This was accomplished by varying the velocity, U_∞, pipe diameter, D, and period oscillation, T. Table A.1 shows the simulations performed for this study In addition to the simulation parameters, peak average shear, $\bar{\tau}_p$, *KC*

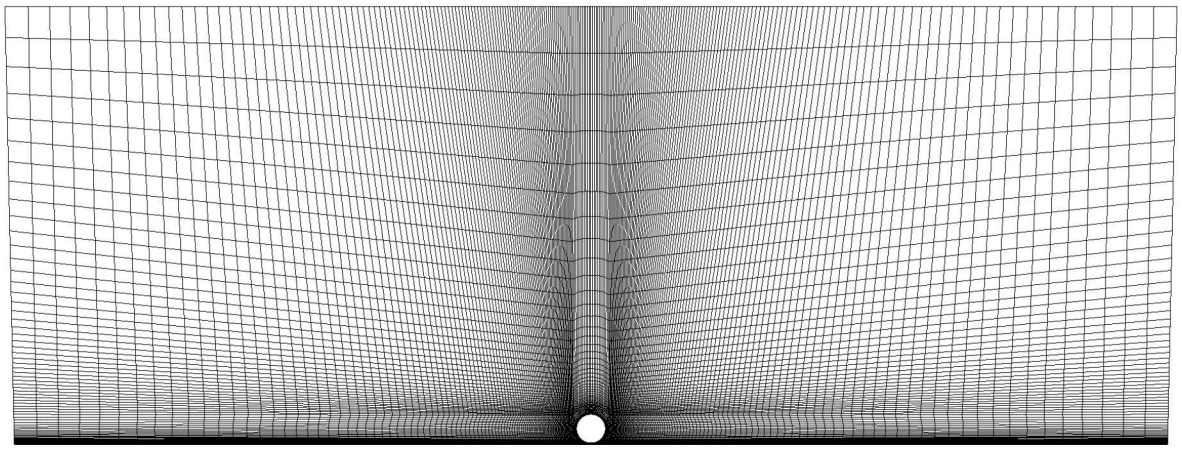

Figure A.2: Computational grid used for numerical analysis.

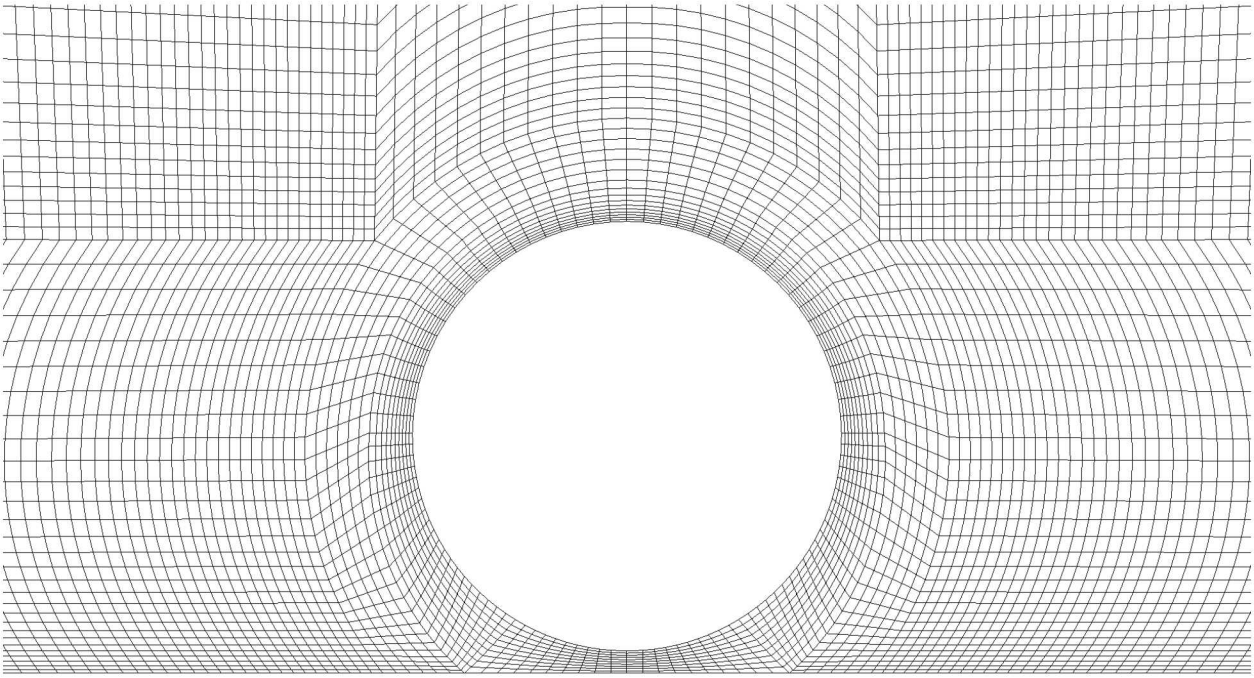

Figure A.3: Close up zoom of the numerical grid.

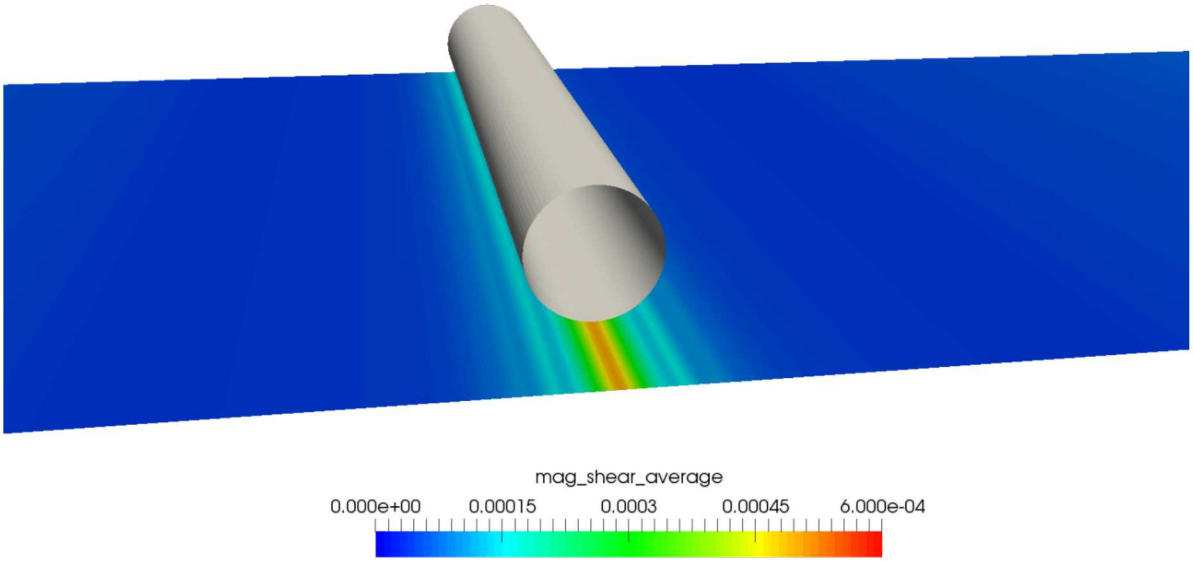

Figure A.4: OpenFOAM results for simulated wave over 2D pipe with $U = 0.4$ m/s and $T = 16$ s.

number, scour depth, S, scour width, W, and a scour parameter to be subsequently discussed, ζ, are presented. As expected, $\bar{\tau}_p$, was observed to be proportional to the velocity squared.

$$\bar{\tau}_p \propto U_\infty^2 \tag{8}$$

Knowing the trend described by (1), we considered a new quantity based on $\bar{\tau}_p$.

$$\zeta = \sqrt{\frac{\bar{\tau}_p T D}{U \rho}} \tag{9}$$

The quantity ζ has dimensions of length.

$$\left(\overbrace{\frac{[\text{mass}]}{[\text{length}][\text{time}]^2}}^{\bar{\tau}_p} \overbrace{\frac{[\text{time}]}{[1]}}^{T} \overbrace{\frac{[\text{length}]}{[1]}}^{D} \overbrace{\frac{[\text{time}]}{[\text{length}]}}^{1/U} \overbrace{\frac{[\text{length}]^3}{[\text{mass}]}}^{1/\rho} \right)^{1/2} = \overbrace{[\text{length}]}^{\zeta} \tag{10}$$

Testing this new quantity, we find that it shows a strong linear correlation with scour. This trend is shown in Figure A.5. Figure A.5 shows data for offsets of $e = 0.05, 0.1$ m, shown in red and blue respectively. A black dashed line (with $r^2 = 0.988$) in Figure A.5 shows the overall trend. This is given by

Table A.1: 2D flow over pipe cases considered for this study.

Offset, e [m]	Diam., D [m]	Vel., U [m/s]	Per., T [s]	Shear, $\bar{\tau}_p$ [Pa]	KC []	S [m]	W [m]	ζ [m]
0.05	1	0.4	16.0	6.27×10^{-4}	6.4	0.25	1.17	0.16
0.05	1	0.8	8.0	2.12×10^{-3}	6.4	0.25	1.17	0.15
0.05	1	1.0	6.4	3.19×10^{-3}	6.4	0.25	1.17	0.14
0.05	1	1.2	20.0	5.50×10^{-3}	24.0	0.49	2.76	0.30
0.05	1	2.0	16.0	1.44×10^{-2}	32.0	0.57	3.33	0.34
0.05	1	0.5	16.0	9.70×10^{-4}	8.0	0.28	1.35	0.18
0.05	1	1.0	20.0	3.88×10^{-3}	20.0	0.45	2.45	0.28
0.05	1	2.0	16.0	1.44×10^{-2}	32.0	0.57	3.33	0.34
0.10	1	0.4	16.0	4.64×10^{-4}	6.4	0.25	1.17	0.14
0.10	1	0.8	8.0	1.37×10^{-3}	6.4	0.25	1.17	0.12
0.10	1	1.0	6.4	2.05×10^{-3}	6.4	0.25	1.17	0.11
0.10	1	1.2	20.0	5.18×10^{-3}	24.0	0.49	2.76	0.29
0.10	2	2.4	20.0	1.85×10^{-2}	24.0	0.98	5.52	0.56
0.10	1	2.0	16.0	1.36×10^{-2}	32.0	0.57	3.33	0.33
0.10	1	0.5	16.0	7.94×10^{-4}	8.0	0.28	1.35	0.16
0.10	1	1.0	20.0	3.62×10^{-3}	20.0	0.45	2.45	0.27
0.10	1	2.0	16.0	1.36×10^{-2}	32.0	0.57	3.33	0.33
0.10	2	0.5	16.0	7.32×10^{-4}	4.0	0.40	1.72	0.22
0.10	2	1.0	20.0	3.41×10^{-3}	10.0	0.63	3.13	0.37
0.10	2	1.6	20.0	8.49×10^{-3}	16.0	0.80	4.24	0.46
0.10	1	0.1	10.0	2.91×10^{-5}	1.0	0.10	0.35	0.05

$$S = 1.6706\zeta + 0.0141. \tag{11}$$

The high degree of accuracy in this trend essentially affirms that $\tau \propto U^2$. However, the coefficients in (11) are specific to flow under a pipe-like body.

Note that ζ is defined partially by some characteristic dimension, D. This parameter, while somewhat inconvenient, is believed to incorporate the some connection to turbulence scale, which is known to be an important factor for scour in waves [3]. In order to apply (9) to some arbitrary geometry, a single characteristic length, D, must be defined.

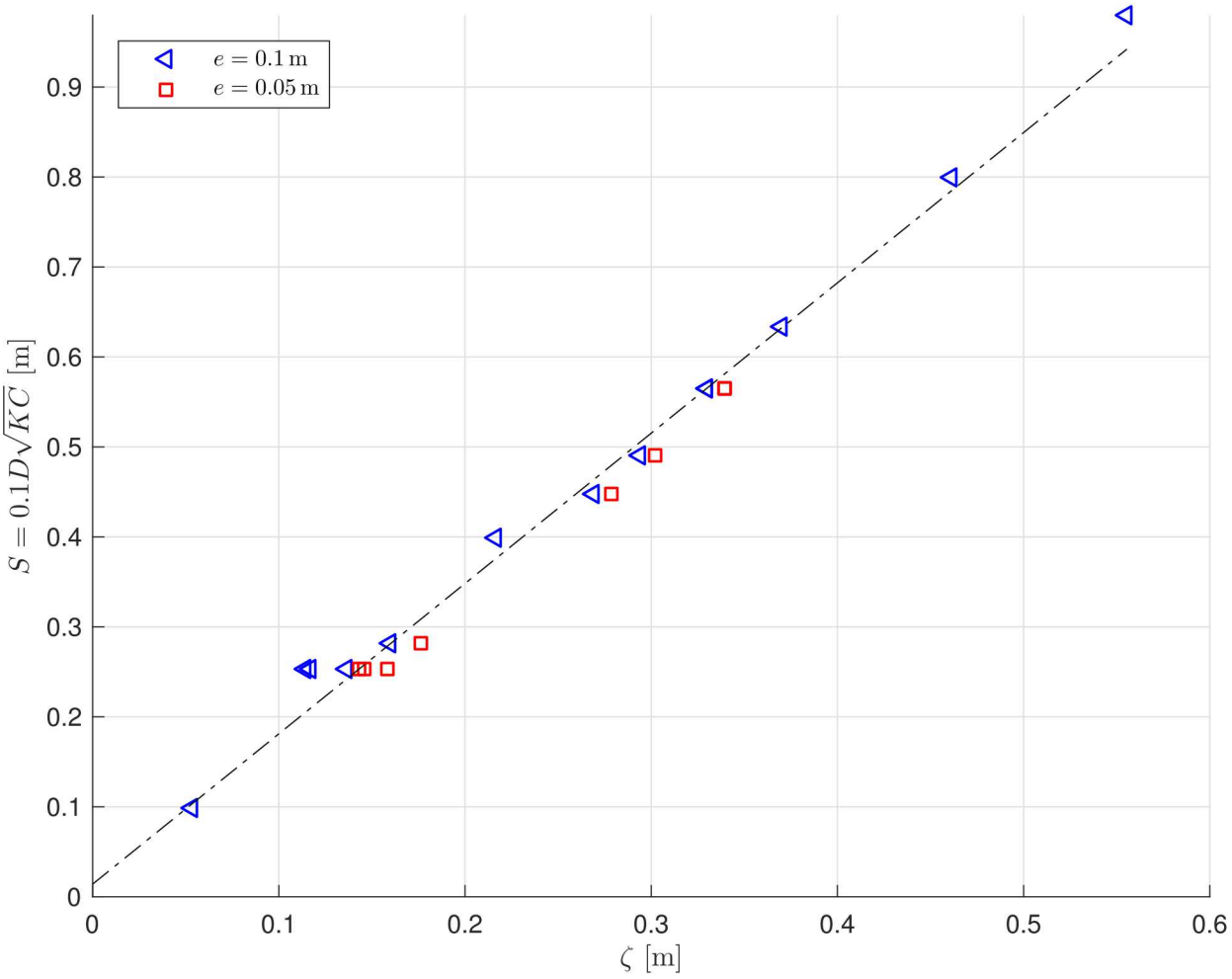

Figure A.5: Correlation of peak shear stress quantity, $\zeta = \sqrt{\frac{\bar{\tau}_p TD}{U\rho}}$, and scour, $S = 0.1D\sqrt{KC}$. Linear trend of $S = 1.6706\zeta + 0.0141$ has $r^2 = 0.988$.

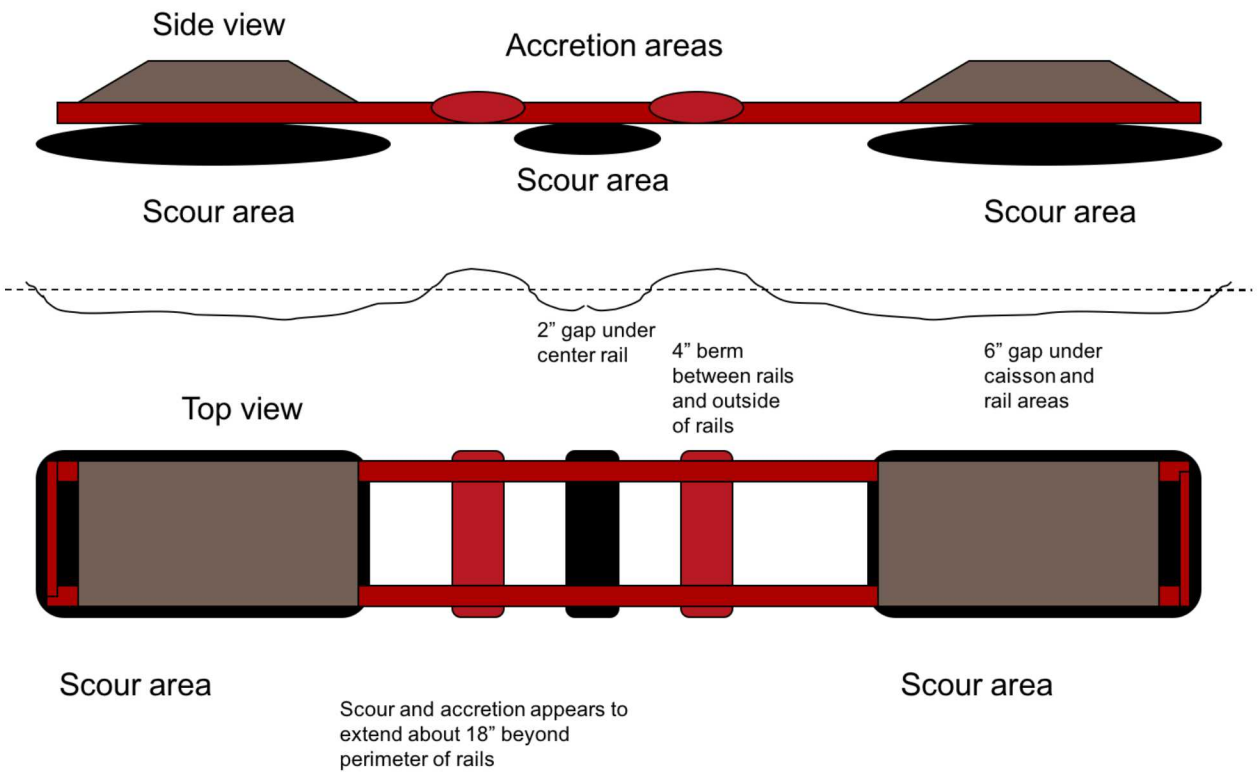

Figure B.6: Qualitative scour under M3 Apex device based on at-sea deployment.

B Apex CFD scenes

In order to assess the ability of the trend developed in Section 3, here we consider the M3 Apex device. An at-sea deployment was conducted with the Apex device. During this deployment, the device was subjected to a wide range of wave conditions. In addition to variation in spectral content, the wave heading also varied during this deployment. Additionally, the sediment on which the device was situated for this deployment was non-homogeneous. Qualitative observations of this device showed roughly 6 in of scour underneath the frame of the device (see Figure B.6).

The procedure for this assessment utilized the following steps:

1. Perform CFD simulations with M3 Apex device (conditions shown in Table B.2)
2. Knowing that the observed scour was 6 in ($\sim$ 15 cm), reformulate (11) as

$$D = \frac{U\rho}{\tau T}\left(\frac{S-0.0141}{1.6706}\right)^2 \tag{12}$$

3. Find the characteristic dimension, D, using (12) for each CFD simulation
4. Compare the calculated characteristic dimension with the actual dimensions of the M3 device.

Table B.2: Shear-based prediction of scour for M3 Apex.

ID	Offset, e [m]	Velocity, U [m/s]	Period, T [s]	τ_m [Pa]	$\bar{\tau}_p$ [Pa]	$D(\tau_m)$ [m]	$D(\bar{\tau}_p)$ [m]
1	0.01 (A)	0.16	8.3	8.70E-4	4.07E-4	0.152 m (6 in)	0.324 m (12.8 in)
2	.01 (B)	0.4	16	2.18E-3	9.85E-4	0.0784 m (3.1 in)	0.195 m (6.9 in)
3	0.05	0.4	16	2.69E-3	1.17E-3	0.0638 m (2.5 in)	0.146 m (5.7 in)
4	0.1	0.4	16	2.53E-3	1.02E-3	0.0678 m (2.7 in)	0.168 m (6.6 in)

The results of this study are summarized in Table B.2. Note that in addition to the peak of the period-averaged shear stress ($\bar{\tau}_p$), Table B.2 also presents results for the peak of the maximum shear stress (τ_m). Scalar images of $\bar{\tau}_p$ and τ_m are shown in Appendix B. From Table B.2, we can see that for the majority for the cases considered, the characteristic dimension, when using $\bar{\tau}_p$ is close to the $D = 6$ in observed in the at-sea deployment.

This Section contains a number of rendered scenes from CFD simulations of the M3 Apex device. In each figure, the results are shown (clockwise from the upper left) for simulation 1, 2, 3, and 4 in Table B.2.

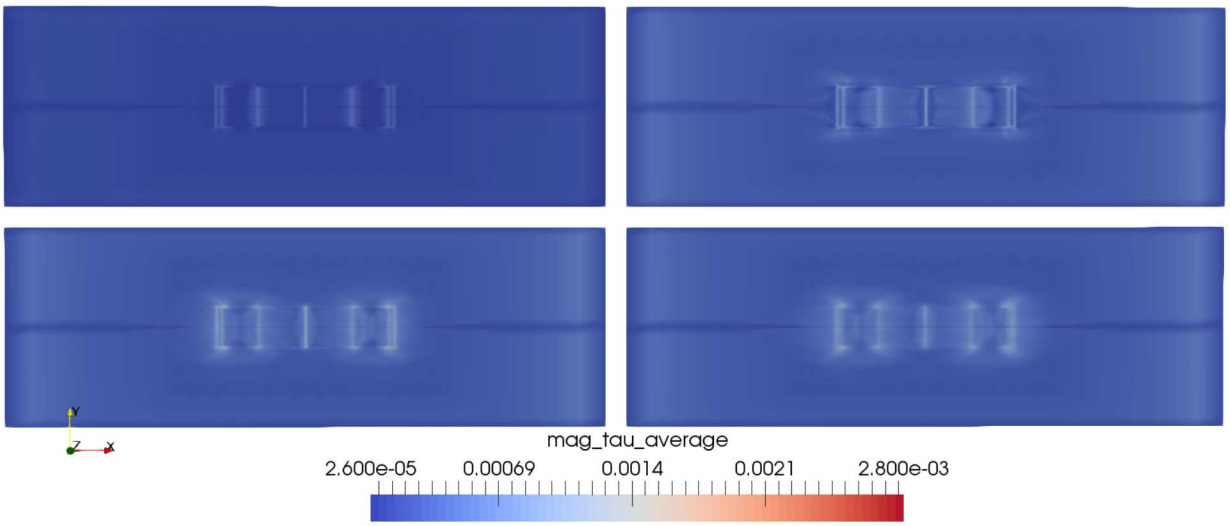

Figure B.7: Comparison of $\bar{\tau}_p$ for M3 Apex simulations listed in Table B.2. Simulation results are shown (clockwise from the upper left) for simulation 1, 2, 3, and 4 in Table B.2.

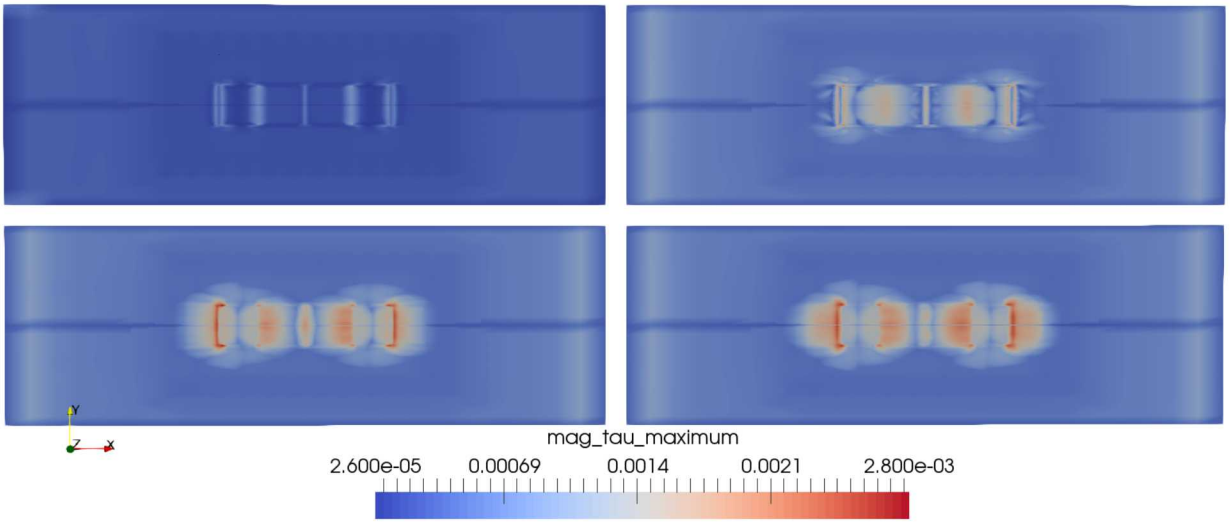

Figure B.8: Comparison of τ_m for M3 Apex simulations. Simulation results are shown (clockwise from the upper left) for simulation 1, 2, 3, and 4 in Table B.2.

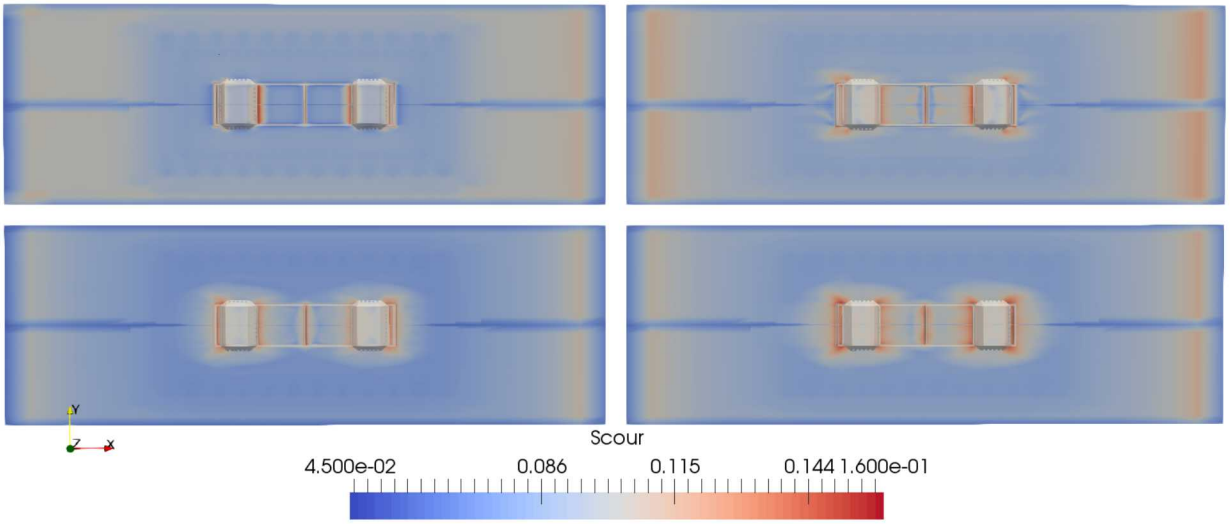

Figure B.9: Scour based on $\bar{\tau}_p$ for M3 Apex simulations. Simulation results are shown (clockwise from the upper left) for simulation 1, 2, 3, and 4 in Table B.2.

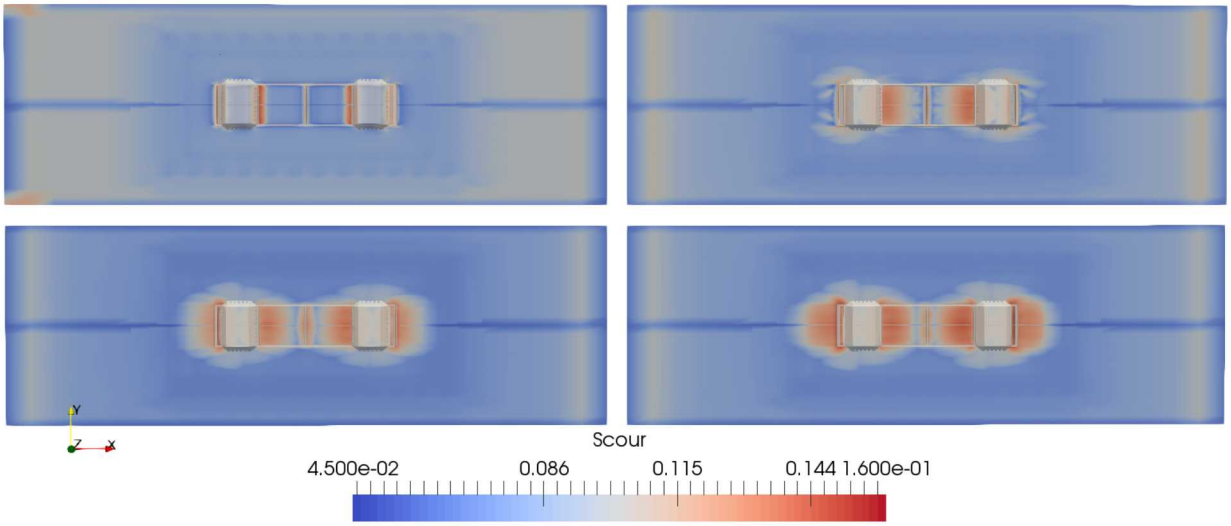

Figure B.10: Scour based on τ_m for M3 Apex simulations. Simulation results are shown (clockwise from the upper left) for simulation 1, 2, 3, and 4 in Table B.2.

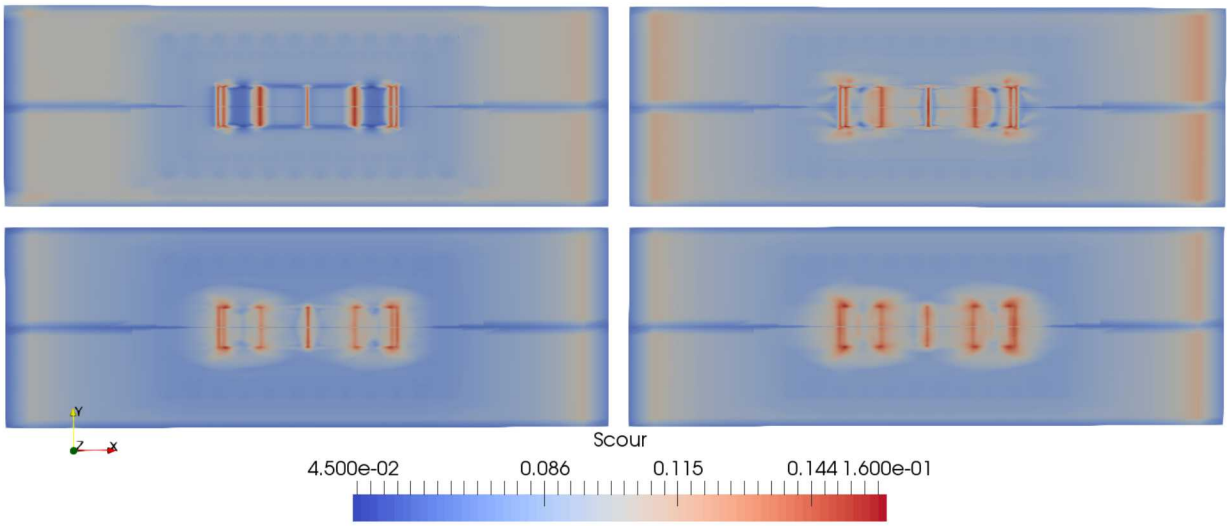

Figure B.11: Scour based on $\bar{\tau}_p$ for M3 Apex simulations (no device shown). Simulation results are shown (clockwise from the upper left) for simulation 1, 2, 3, and 4 in Table B.2.

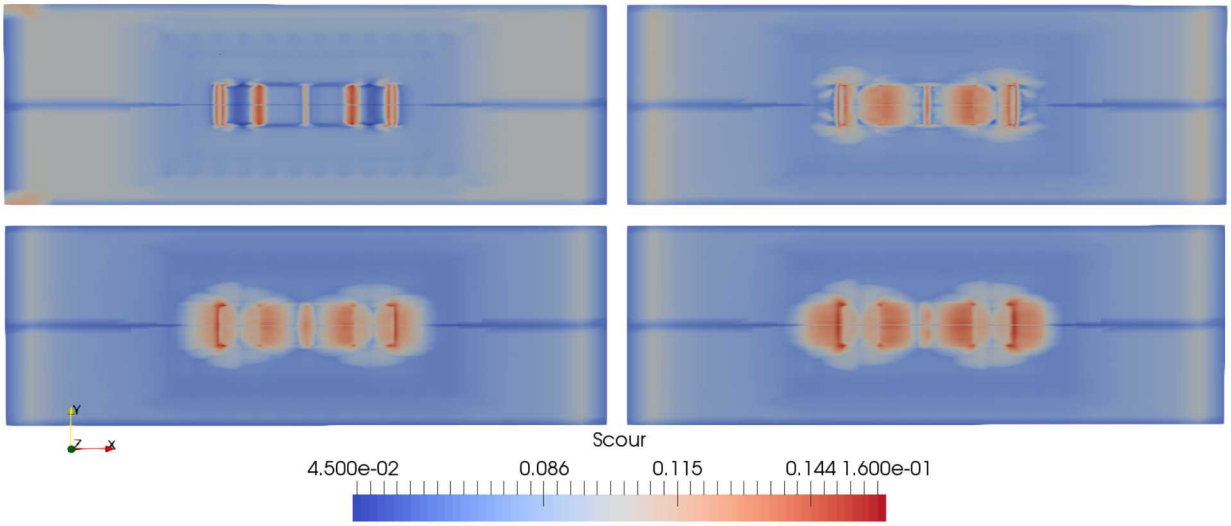

Figure B.12: Scour based on τ_m for M3 Apex simulations (no device shown). Simulation results are shown (clockwise from the upper left) for simulation 1, 2, 3, and 4 in Table B.2.

DISTRIBUTION:

1 MS 0899 Technical Library, 9536 (electronic copy)


Sandia National Laboratories